Supporting Information (SI) for

Co-enhancing interfacial solar-driven evaporation and hydrovoltaic electricity generation by porous carbon nanoparticle from waste polyester

Huiyue Wang, Xueying Wen, Guixin Hu, Hongrun Zhu, Zhikun Dai, Xinyao Zhang, Qianyu Wei, Huajian Liu*, Ran Niu*, Jiang Gong*

Key Laboratory of Material Chemistry for Energy Conversion and Storage, Ministry of Education, Hubei Key Laboratory of Material Chemistry and Service Failure, Hubei Engineering Research Center for Biomaterials and Medical Protective Materials, Semiconductor Chemistry Center, School of Chemistry and Chemical Engineering, Huazhong University of Science and Technology, Wuhan 430074, China.

*Corresponding authors.

E-mail addresses: lhj19858161129@163.com (H. Liu); niuran@hust.edu.cn (R. Niu); gongjiang@hust.edu.cn (J. Gong)

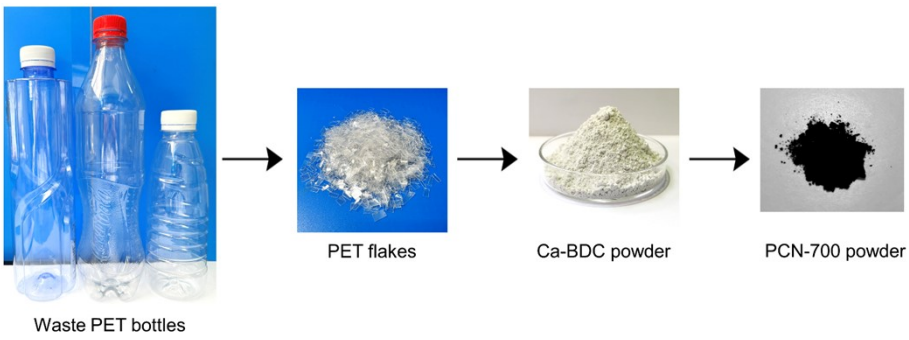

Fig. S1 Preparation of Ca-BDC and PCN-700 from waste PET bottles.

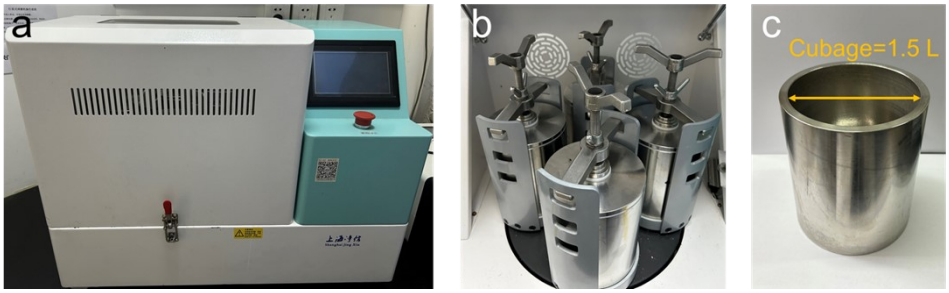

Fig. S2 Photographs of (a) a planetary ball mill (JX-4GL), (b) 4 sealed ball milling jars, and (c) a milling jar (1.5 L).

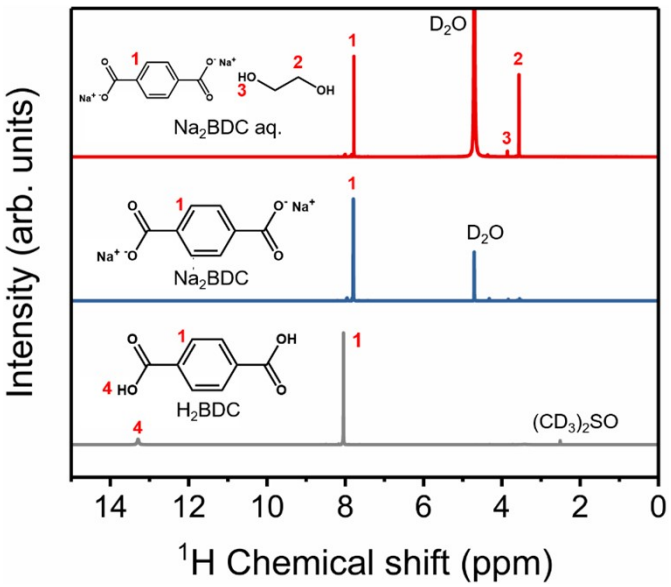

Fig. S3 ^{1}H NMR spectra of Na_2BDC aqueous solution containing ethylene glycol (dissolved in D_2O), Na_2BDC obtained by heating the above aqueous solution (dissolved in D_2O), and the derived H_2BDC powder (dissolved in $(CD_3)_2SO$).

Note: The samples are derived from the Na_2BDC product obtained by ball milling.

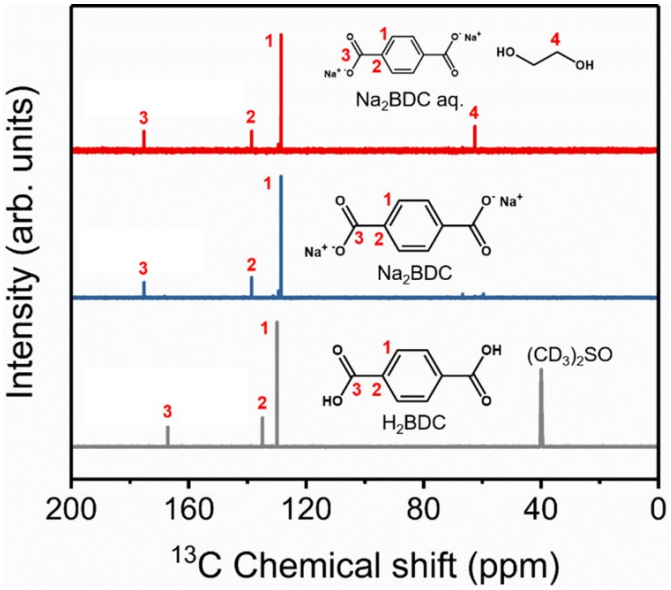

Fig. S4 ^{13}C NMR spectra of Na_2BDC aqueous solution containing ethylene glycol (dissolved in D_2O), Na_2BDC obtained by heating the above aqueous solution (dissolved in D_2O), and the derived H_2BDC powder (dissolved in $(CD_3)_2SO$).

Note: The samples are derived from the Na_2BDC product obtained by ball milling.

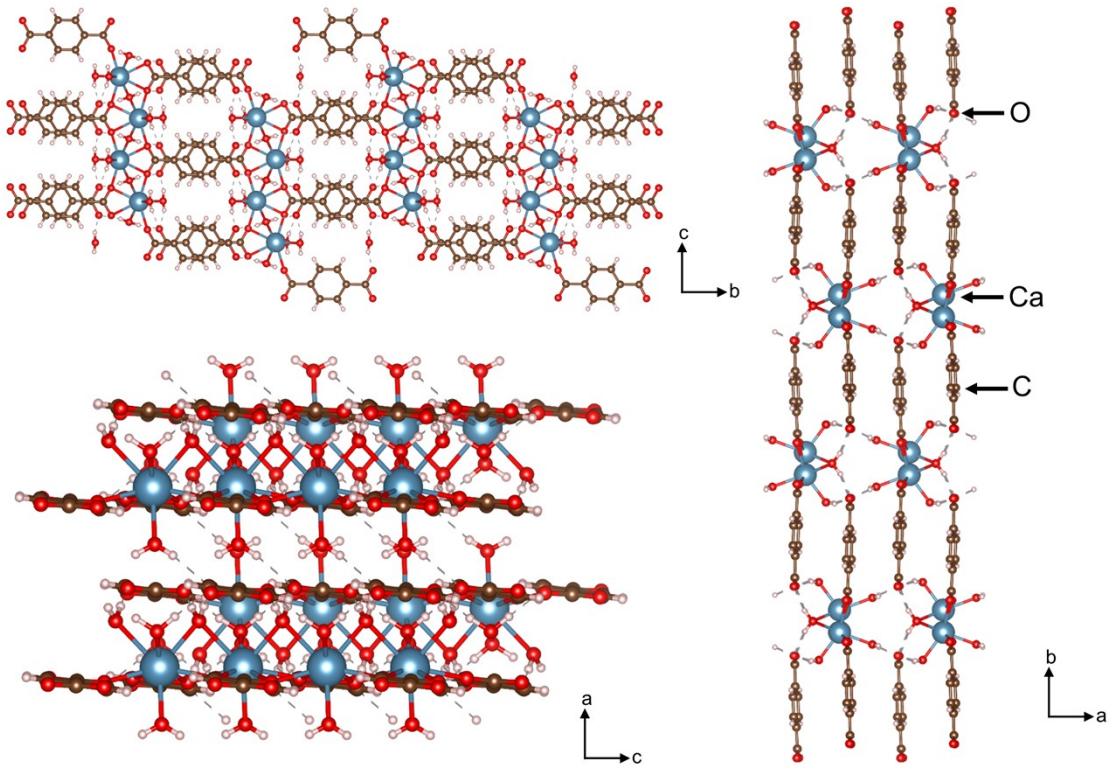

Fig. S5 Schemes of Ca-BDC from different dimensions.

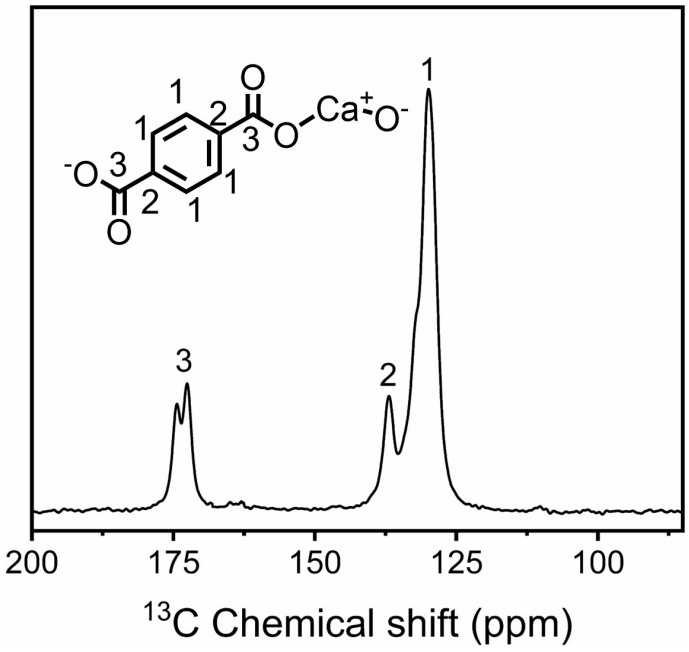

Fig. S6 Solid-state ^{13}C NMR spectrum of Ca-BDC.

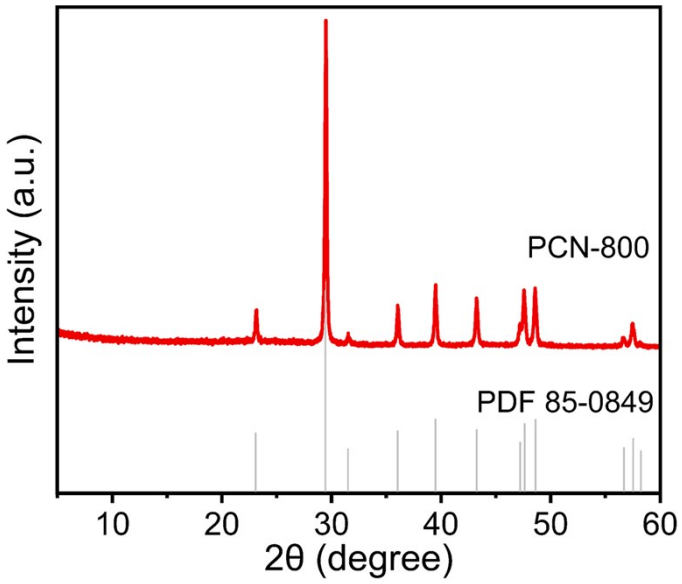

Fig. S7 XRD patterns of PCN-800 before purification as well as talcum carbonate (PDF 85-0849).

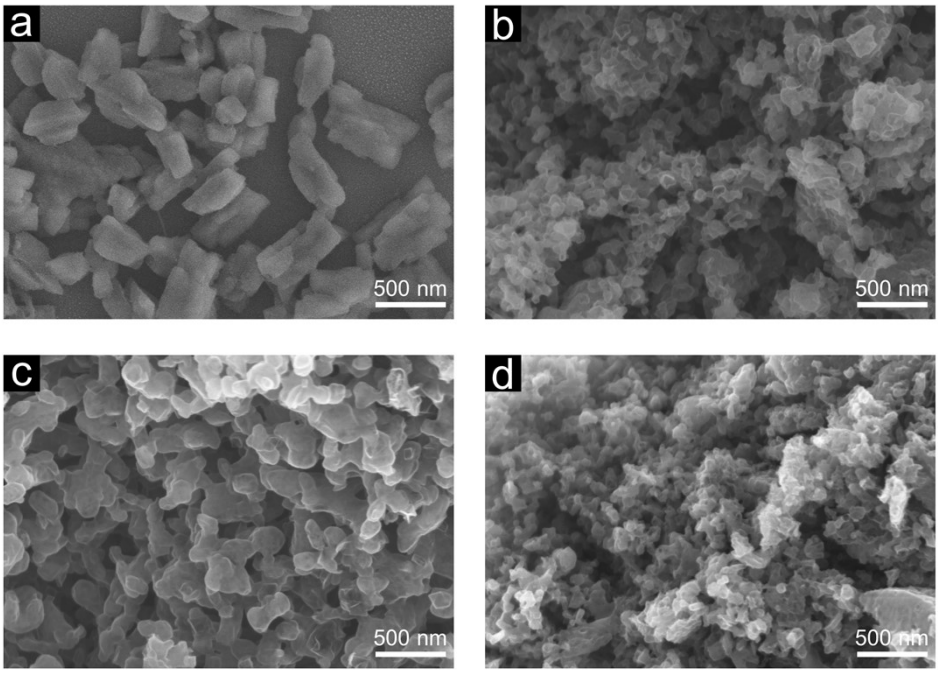

Fig. S8 SEM images of (a) Ca-BDC, (b) PCN-600, (c) PCN-700, and (d) PCN-800.

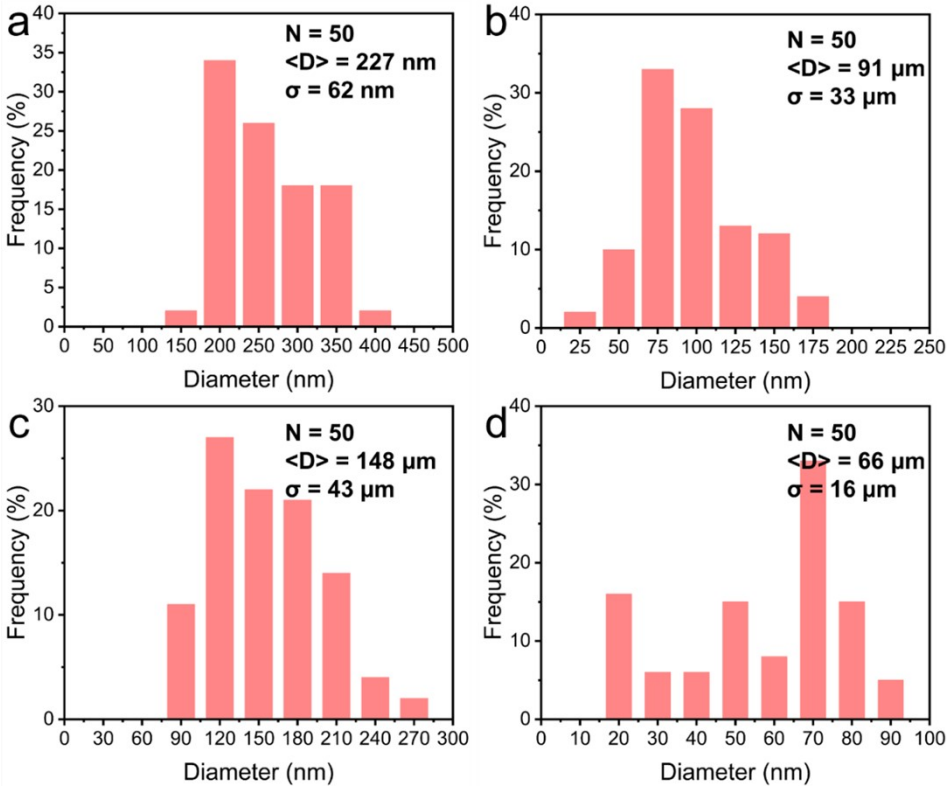

Fig. S9 Diameter distribution plots of (a) Ca-BDC, (b) PCN-600, (c) PCN-700, and (d) PCN-800.

Note: *N* refers to the number of samples, <*D*> refers to the mean diameter, and σ refers to the standard deviation.

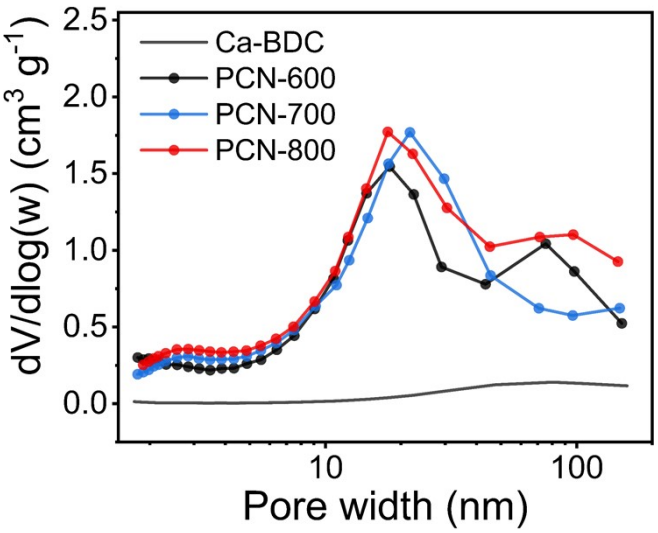

Fig. S10 N_2 adsorption/desorption isotherms of Ca-BDC and PCN-*x* with pore size distribution curves calculated using BJH model.

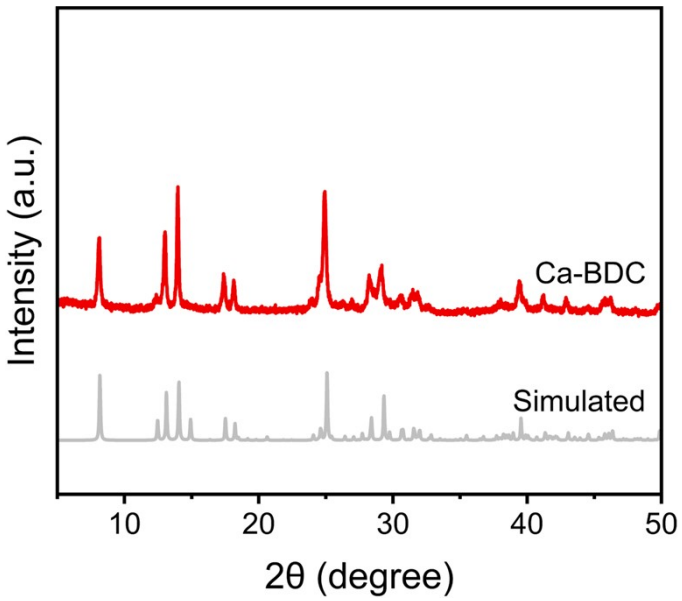

Fig. S11 XRD pattern of Ca-BDC compared to the simulated pattern of Ca-BDC.

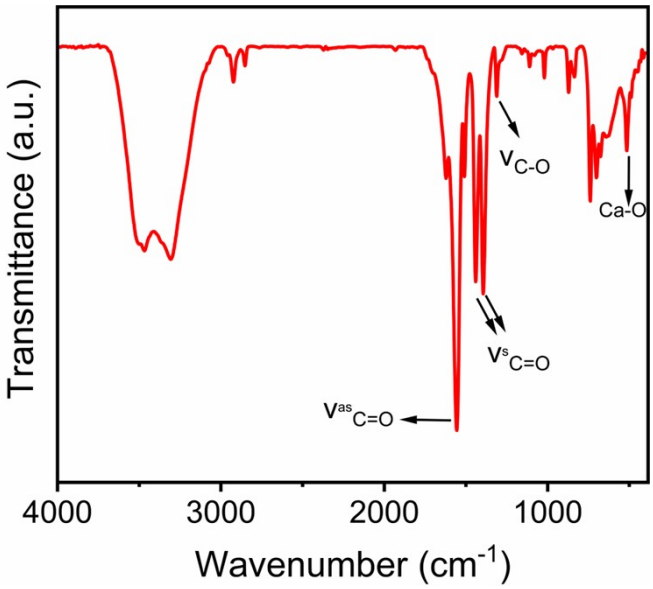

Fig. S12 FT-IR curve of Ca-BDC.

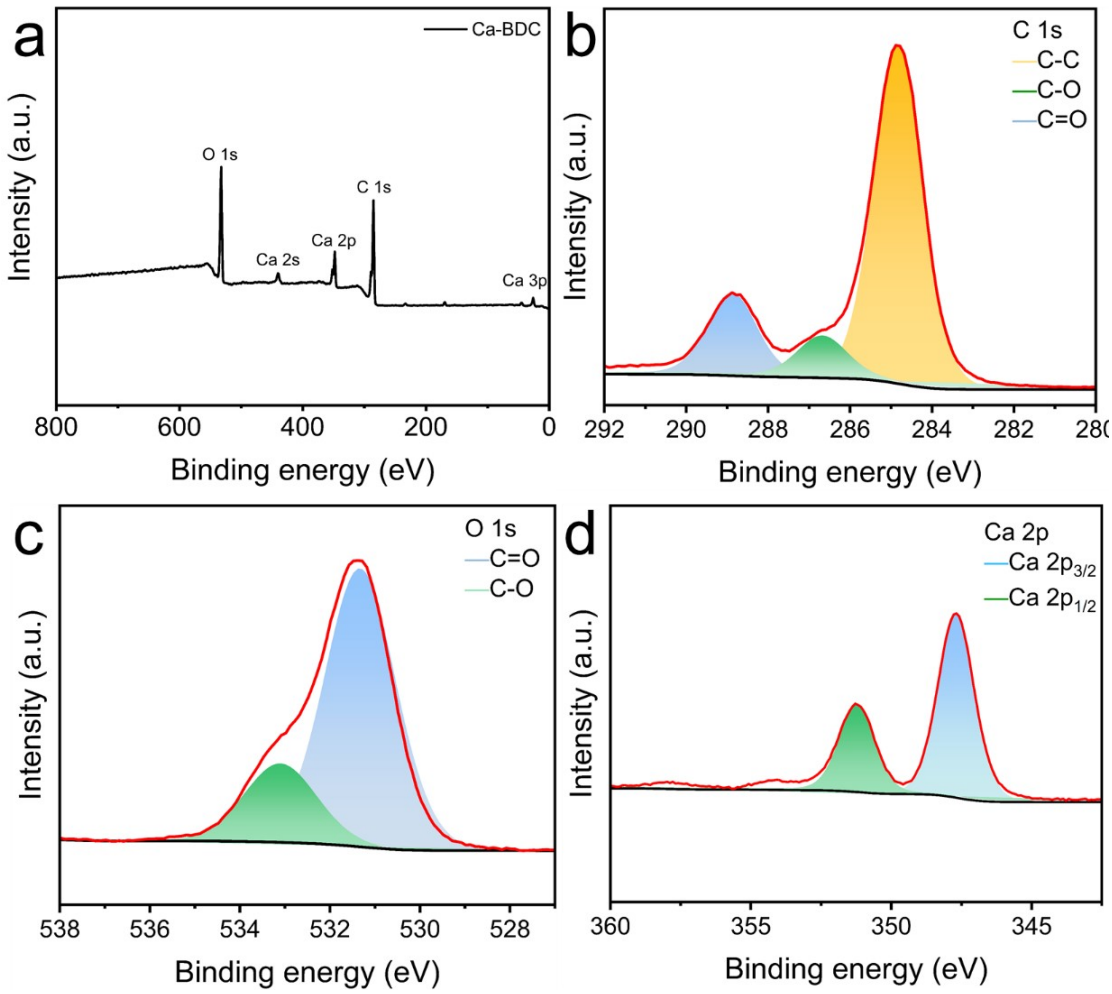

Fig. S13 (a) XPS spectrum of Ca-BDC. High-resolution (b) C 1s, (c) O 1s, and (d) Ca 2p XPS spectra of Ca-BDC.

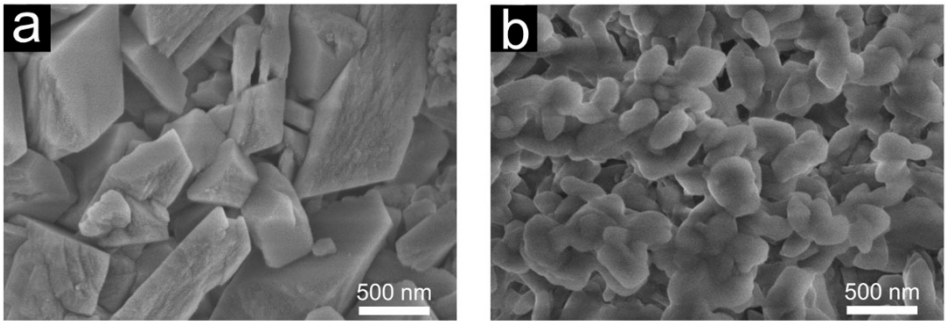

Fig. S14 SEM images of (a) Ba-BDC and (b) Mg-BDC.

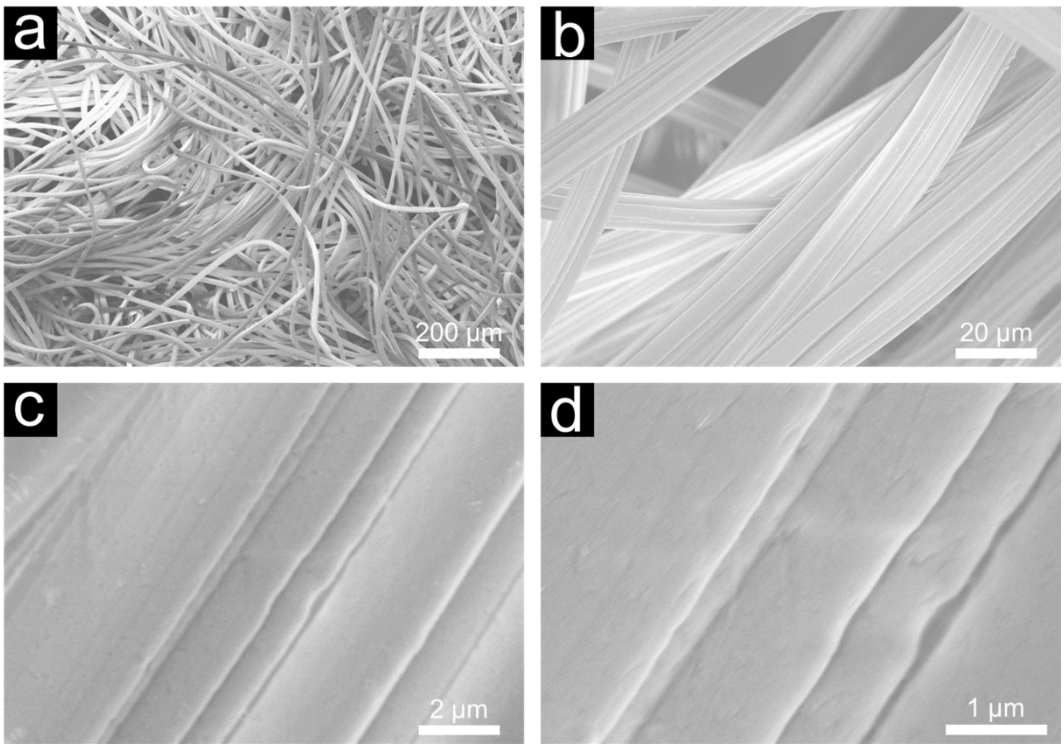

Fig. S15 (a-d) SEM images of non-woven cotton cloth in different magnifications.

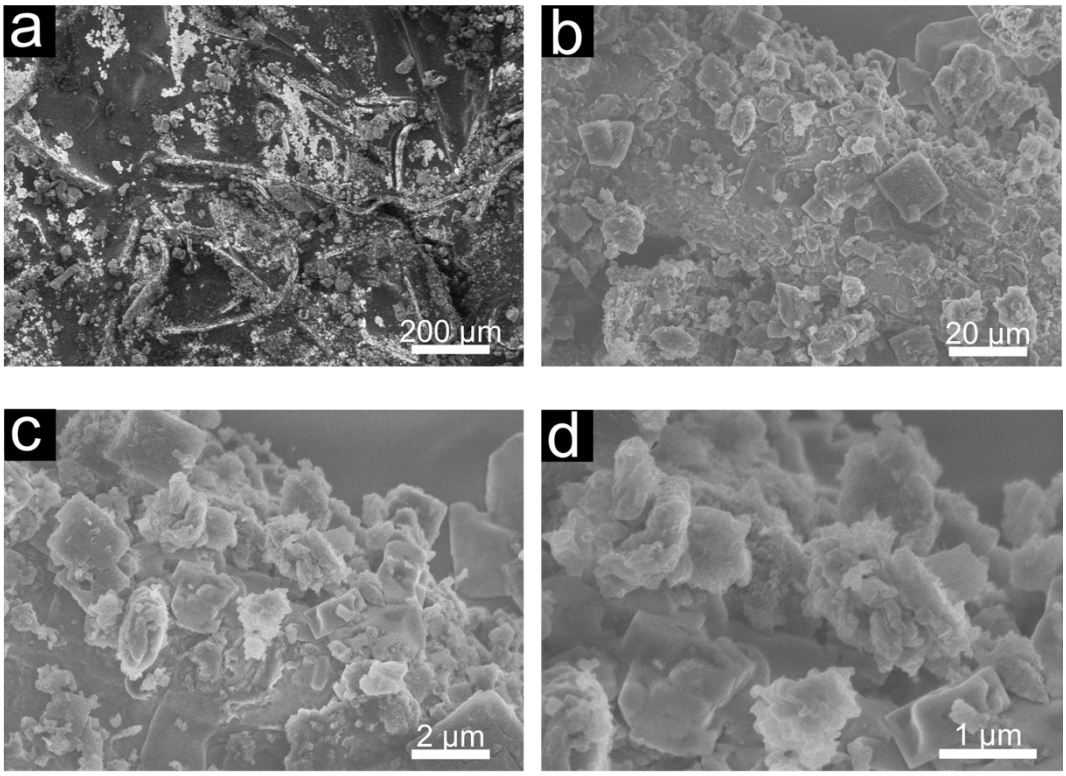

Fig. S16 (a-d) SEM images of PCN-600 evaporator in different magnifications.

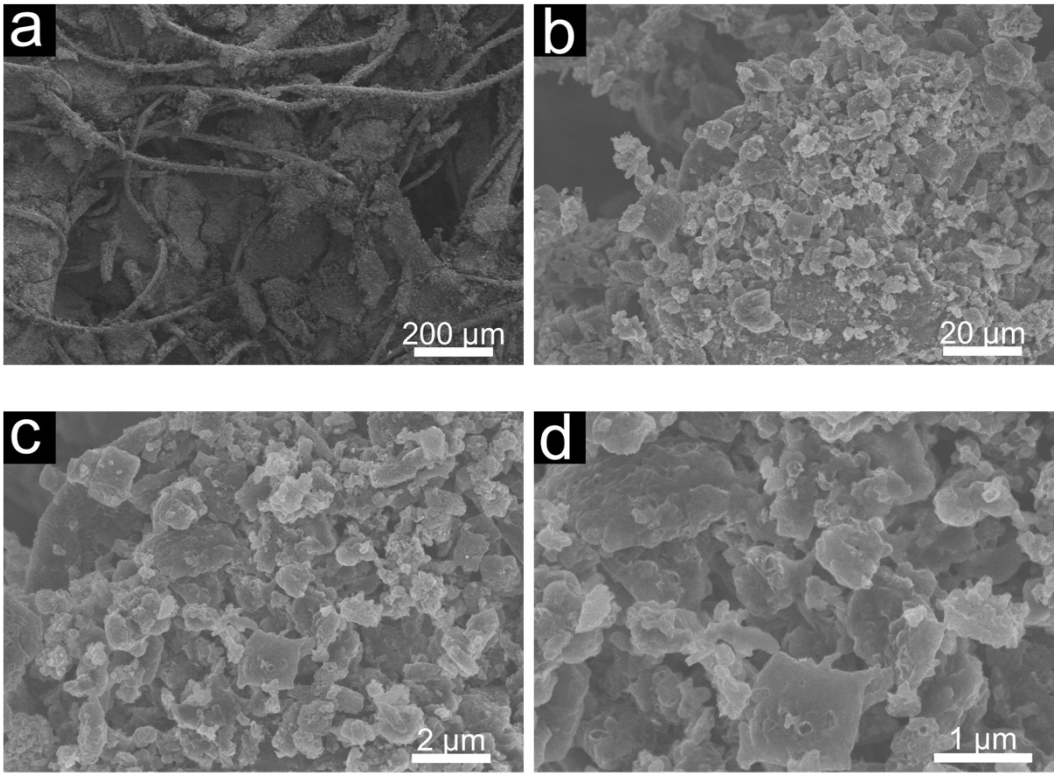

Fig. S17 (a-d) SEM images of PCN-700 evaporator in different magnifications.

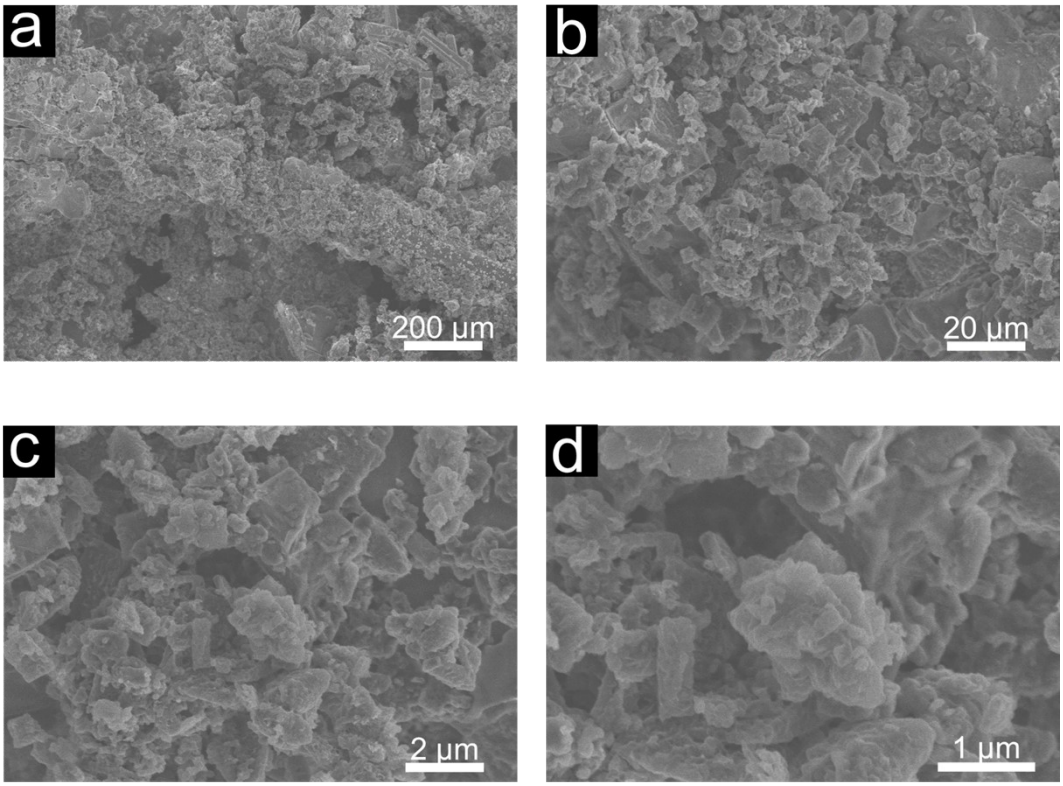

Fig. S18 (a-d) SEM images of PCN-800 evaporator in different magnifications.

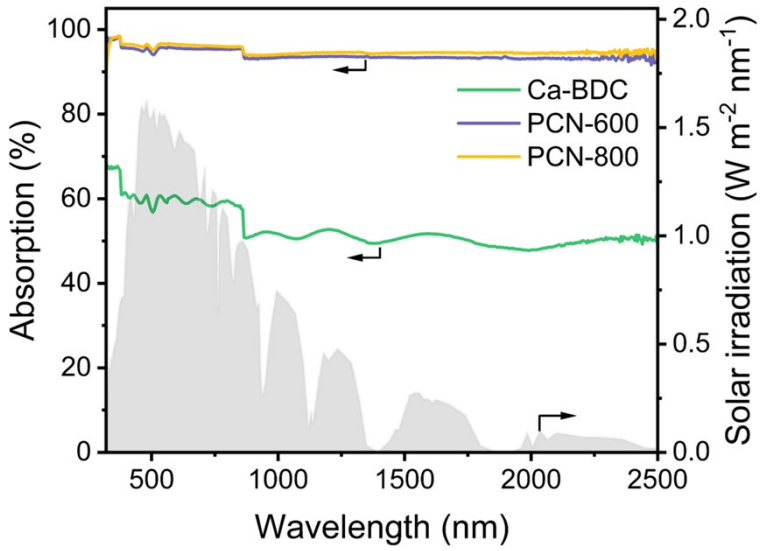

Fig. S19 UV-Vis-NIR absorption spectra of cotton, Ca-BDC, PCN-600, and PCN-800 evaporators.

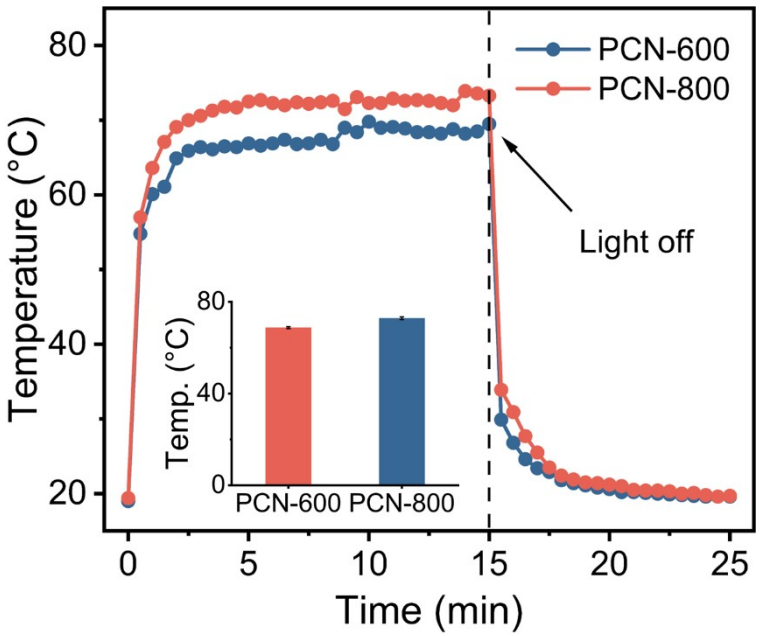

Fig. S20 The surface temperature of PCN-600 and PCN-800 evaporators (1 Sun).

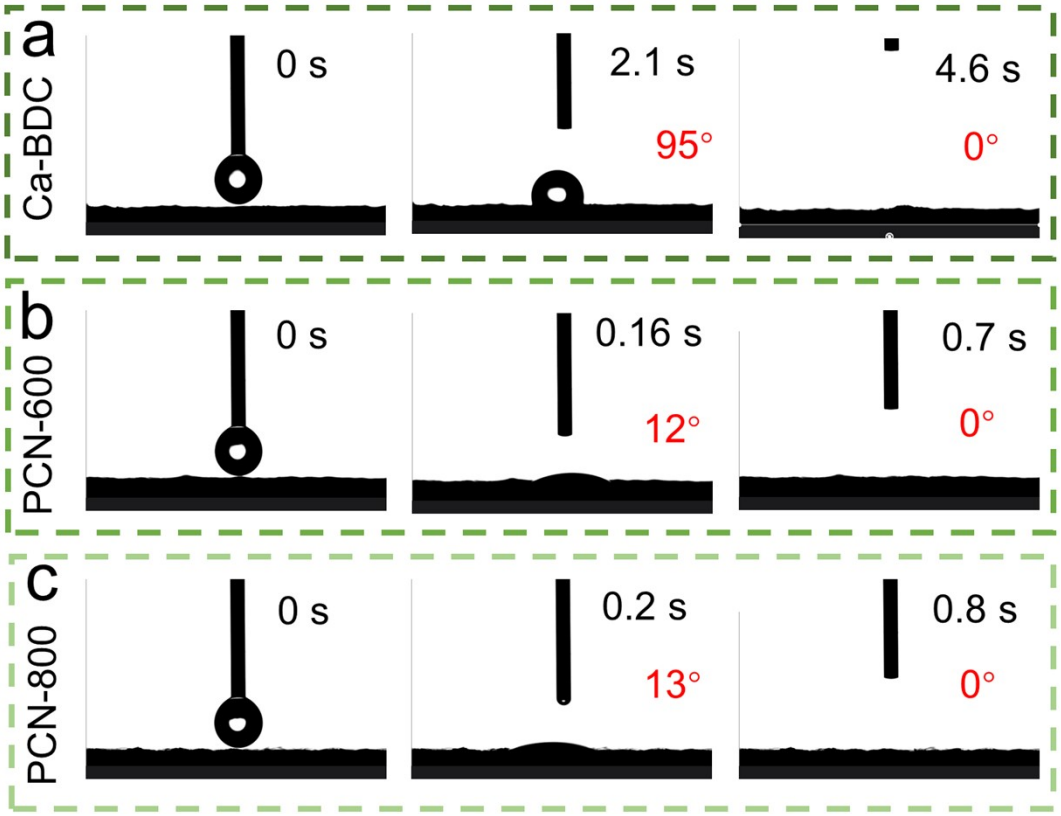

Fig. S21 Water contact angles of (a) Ca-BDC, (b) PCN-600, and (c) PCN-800 evaporators.

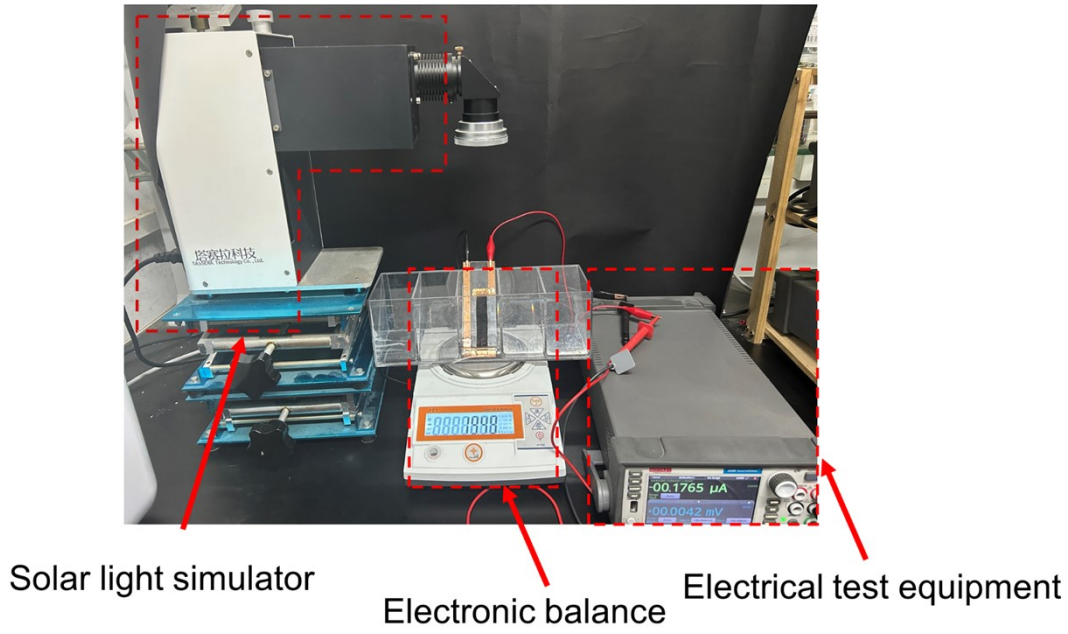

Fig. S22 Photograph of the interfacial solar steam generation system in this work.

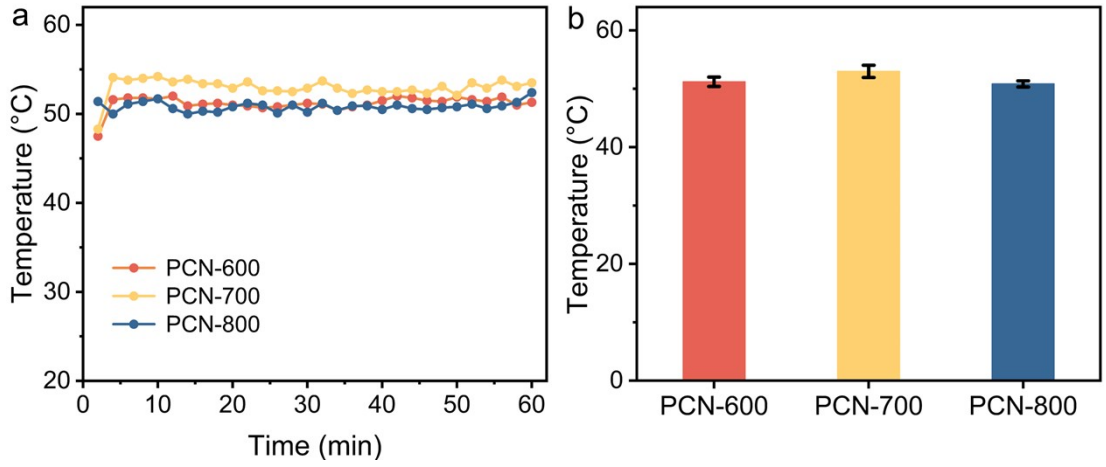

Fig. S23 (a) The variation of surface temperature of PCN-*x* evaporators during evaporation. (b) The comparison of the surface temperature of PCN-*x* evaporators.

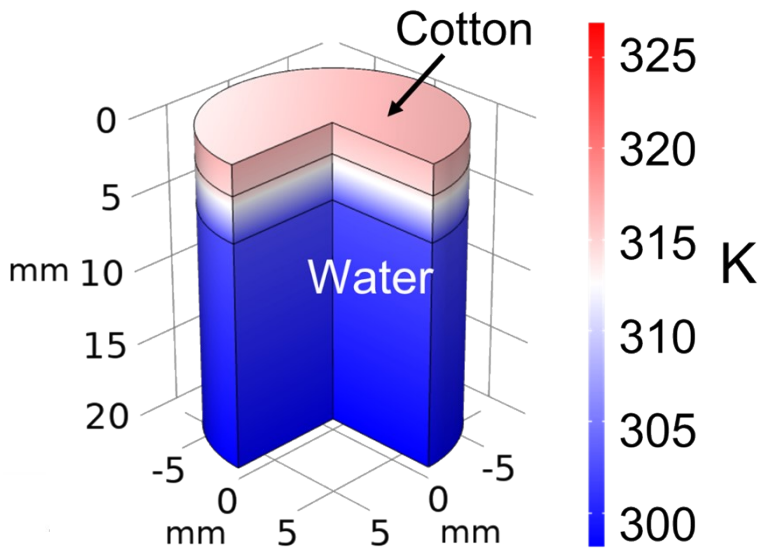

Fig. S24 COMSOL simulation of cotton evaporator.

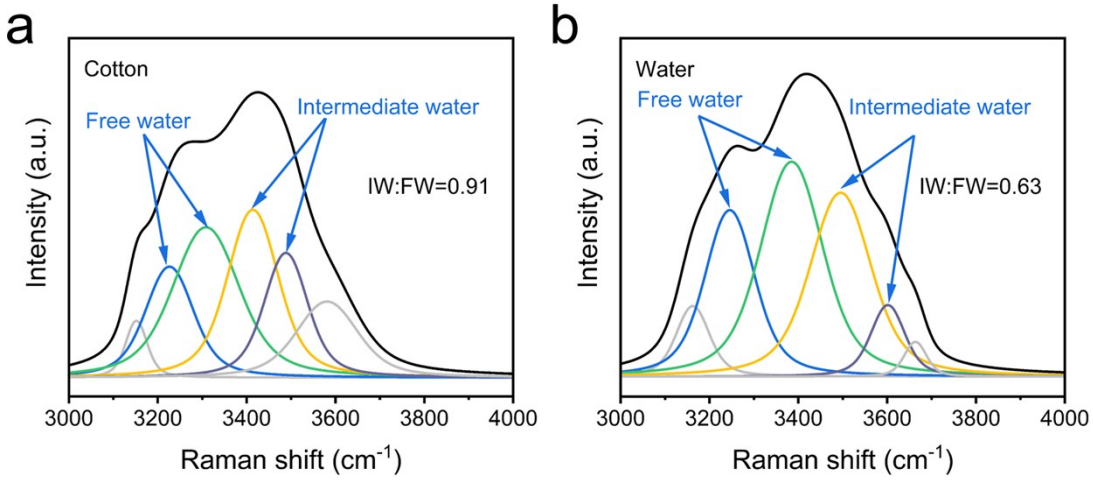

Fig. S25 Raman spectra of (a) cotton and (b) pure water with the fitted peaks showing IW and FW.

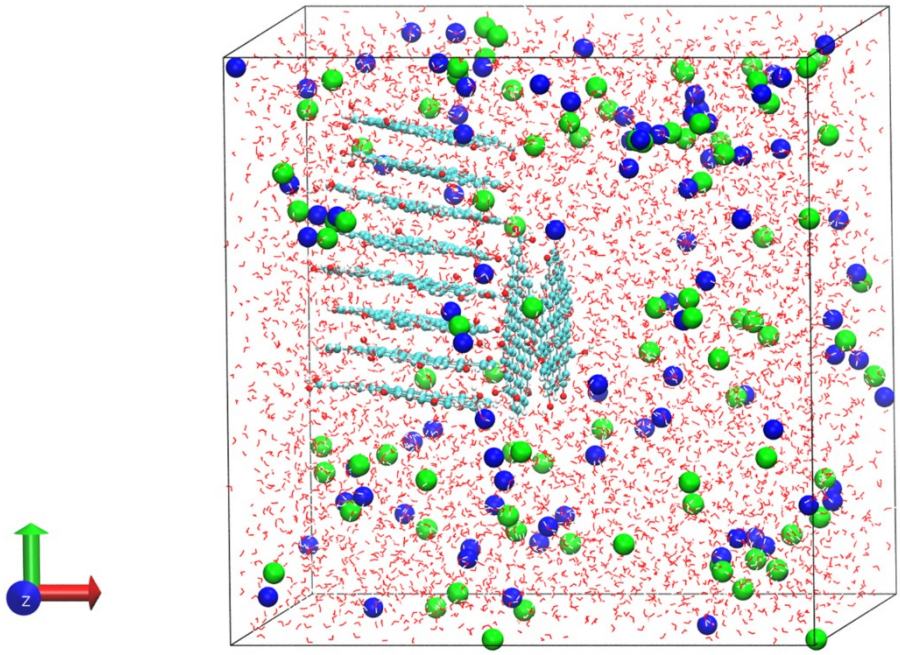

Fig. S26 Molecular dynamics simulation of equilibrium state diagrams.

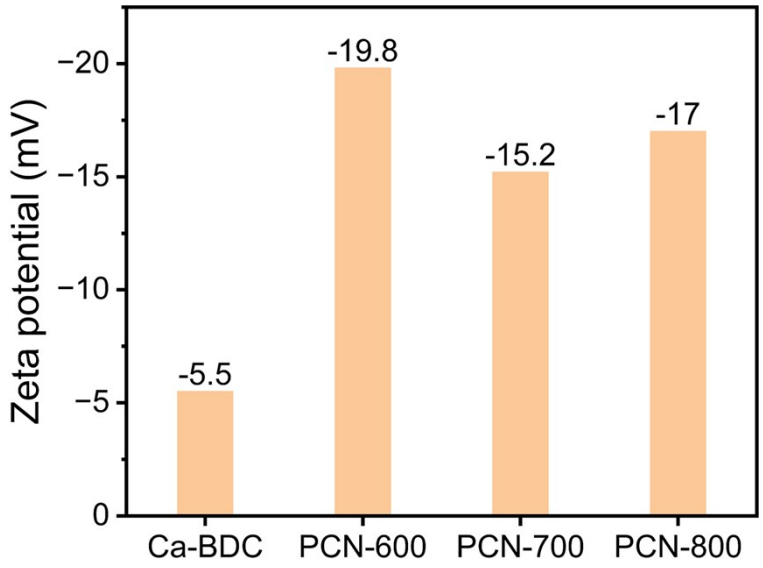

Fig. S27 Zeta potential of Ca-BDC, PCN-600, PCN-700, and PCN-800 in water.

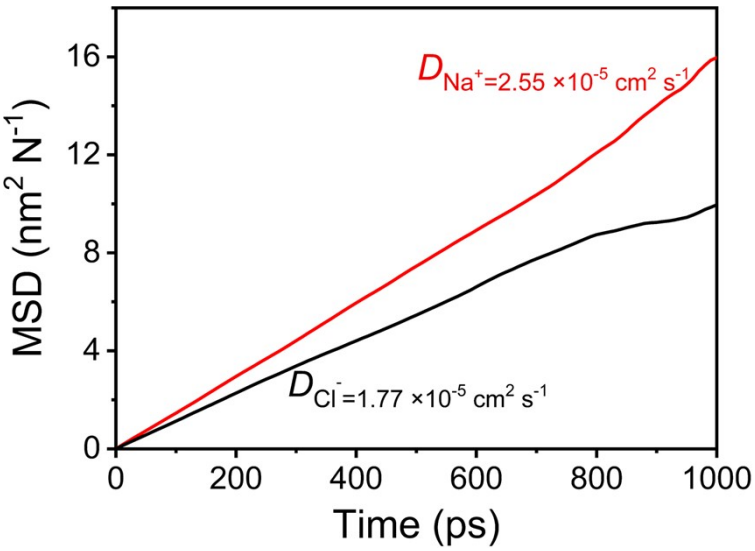

Fig. S28 Na^+ and Cl^- diffusion rate plots during last 1 ns.

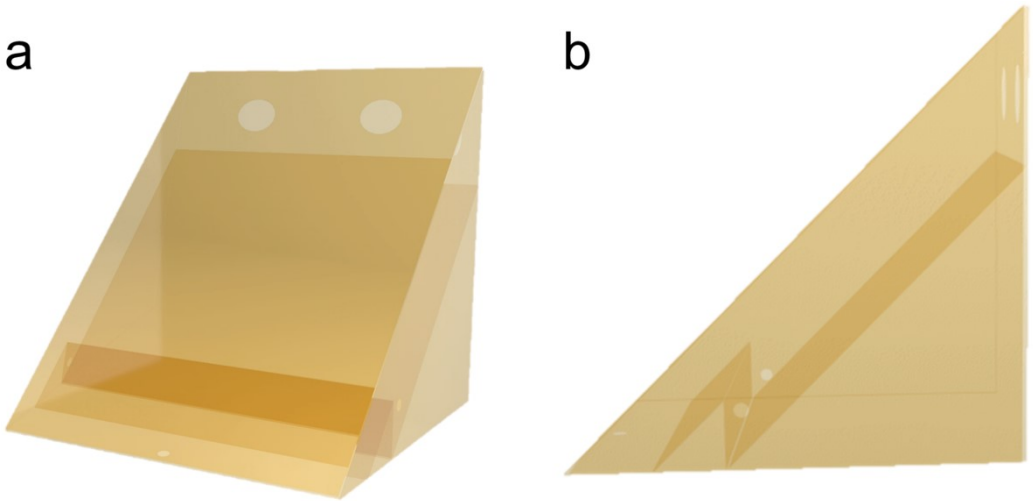

Fig. S29 Model diagram of the outdoor installation.

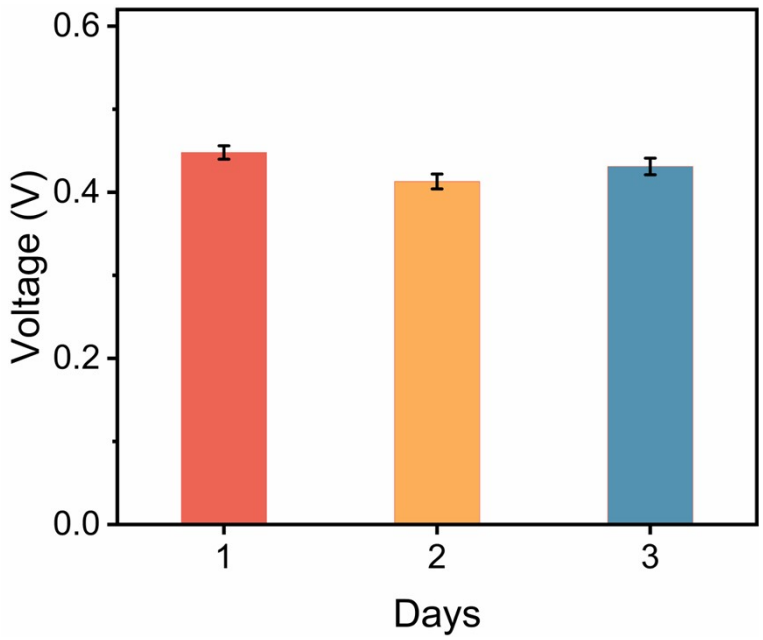

Fig. S30 The average output voltage in electricity generation practical experiment using the PCN-700 evaporator.

Table S1 XPS results of Ca-BDC and PCN-*x* (*x* = 600, 700 and 800).

Element	Content (%)			
	Ca-BDC	PCN-600	PCN-700	PCN-800
C	64.94	94.26	95.36	95.56
O	29.59	5.56	4.49	4.31
Ca	5.47	0.18	0.15	0.14

Table S2 Comparison of the interfacial solar steam generation performance of the PCN-700 evaporator with some recently reported photothermal materials under 1 kW m^{-2} irradiation.

Entry	Photothermal material	Evaporation flux (kg m^{-2} h^{-1})	Efficiency (%)	Reference in SI
1	**PCN-700 evaporator**	**2.32**	**90.7**	**This work**
2	PCC-800	2.49	90.8	[1]
3	Porous carbon coated wood	2.38	88	[2]
4	Co-MOF/CNT membrane	2.25	89.1	[3]
5	GR/PPy aerogel	2.07	96.3	[4]
6	Sea urchin-like MOF	2.07	91.5	[5]
7	Porous carbon/paper pulp fiber	1.80	87.6	[6]
8	TiO_2/nickel foam	1.25	78.5	[7]
9	Bi-MOF	2.16	87.5	[8]
10	CDW@MOF	1.81	89	[9]
11	MT-Ag_2S/CAM	1.80	91.6	[10]
12	CCS STE	1.58	82	[11]
13	Ag/$MgFe_2O_4$@SCW	1.55	88.6	[12]

14	SA-H@CP	1.36	85	[13]
15	TPA-SBTQ	1.337	92	[14]
16	FR@EC/rGO	1.83	94.2	[15]

Table S3 Comparison of voltage and evaporation flux with some recently reported materials.

Entry	Material	Voltage (mV)	Evaporation flux (kg m^{-2} h^{-1})	Reference in SI
1	**PCN-700 device**	**330**	**2.32**	**This work**
2	Chiber@CNT/rGO-60	260	2.1	[16]
3	MGM@PVDF/SA	219	1.3	[17]
4	PCC-800	201	2.49	[1]
5	MnO/C-700	177	2.38	[18]
6	MC30	168	2.24	[19]
7	PMEG	150	2.6	[20]
8	MXene nanosheet	120	3.3	[21]
9	SiNW/SISCF-based	110	2.17	[22]
10	CP@PVA	113	2.96	[23]
11	IENG	90	2.78	[24]
12	Co-NCNT/NF	60	1.65	[25]
13	PCP-600	212	2.74	[26]
14	CB/PVDF	320	1.44	[27]
15	Zn_2O_3/TiO_2	80	1.51	[28]

16	CNTs/carbon fiber foam	105	1.67	[29]
17	CNTP	100	0.84	[30]
18	CBW10	62	1.87	[31]

Table S4 Summary of the enthalpy values measured from dark experiment and DSC measurement.

Condtion	Enthalpy (kJ g^{-1})				
	Pure water	Cotton cloth	PCN-600 evaporator	PCN-700 evaporator	PCN-800 evaporator
Dark experiment	2.434	2.07	1.737	1.694	1.678
DSC measurement	2.159	1.946	1.791	1.907	1.914

Table S5 Distance of the functional group from the ion in the radial distribution function.

	$-C=O-Na^+$	$-C-OH-Na^+$	$-COOH-Na^+$
r	0.244 nm	0.246 nm	0.256 nm
	$-C=O-Cl^-$	$-C-OH-Cl^-$	$-COOH-Cl^-$
r	0.444 nm	0.322 nm	0.306 nm

Note S1 Calculation of evaporation flux and conversion efficiency

The interfacial solar-driven steam generation system consisted of a solar light simulator (PLS-SXE300E) along with a UV enhanced total reflection filter as the source of light and an electronic balance (JA2003) to accurately measure the change in water mass in real time. The surrounding temperature and relative humidity were

approximately 39 ℃ and 33%, respectively. An infrared camera (DMI220) was used to collect photos of the surface temperature and thermal distribution of evaporators. The water evaporation flux (kg m^{-2} h^{-1}) and photothermal conversion efficiency (η, %) were listed as follows,

$$m = \Delta m/(S \times t)\#(S1)$$

$$\eta = m^{'} \times h_{LV}/(3600 \times P_{in})\#(S2)$$

where Δm stands for the water mass loss in 1 h (kg), S represents the lighting area of the evaporator (6.15×10^{-2} m^2), t refers to the irradiation time (1 h), m' presents the evaporation flux that subtracts the darkroom evaporation flux, h_{LV} represents the water evaporation enthalpy (kJ kg^{-1}), and P_{in} stands for the illumination intensity (kW m^{-2}). Note: We could adjust the current density of the solar simulator and/or the distance between simulated sunlight emitter and the surface of evaporators to change the irradiation intensity.

Note S2 Characterization

Chemical structure was investigated using solid-state ^{13}C nuclear magnetic resonance (NMR, Bruker 400 M spectrometer). Crystalline structure was analyzed using X-ray diffraction (XRD, SmartLab-SE, Japan) and a laser confocal Raman microscope (LabRAM HR800). Specific surface area and pore structure were assessed using a surface area analyzer (Micromeritics ASAP 2460) and analyzed using density functional theory (DFT) or Barret-Joyner-Halenda (BJH) model. The surface elements and functional groups were measured by Fourier transform infrared spectroscopy (FT-IR, INVENIO-R) and X-ray photoelectron spectroscopy (XPS, Thermo ESCALAB 250XI apparatus). The light absorption was tested by using UV-Vis-NIR spectrophotometer (Lambda 750 S). Water contact angle was measured using the Dataphysics OCA15EC. Heat conductivity was measured using a thermal conductivity tester (Hot Disk, model TPS 2500). The evaporation enthalpy was monitored using a differential scanning calorimeter (DSC, DSC2500). Zeta potential was measured by BeNano180 Zeta instrument.

Note S3 COMSOL simulation

The simulated 3D models were established based on the actual PCN-700 evaporator system, which mainly consisted of PCN-700 evaporator, PS foam, and bulk water. The upper hollow cylinder with 20 mm in height and 5 mm in radius was simulated to the membrane evaporator, the middle core cylinder with 3 mm in height and 5 mm in radius was simulated to the floating PS foam, and the remainder of a whole cylinder with 15 mm in height and 5 mm in radius was simulated to the bulk water. Subsequently, the temperature distribution was described as the following equations,

$$E_{in} = \rho C_p \frac{\partial T}{\partial t} + \rho C_p u \cdot \nabla T + \nabla \cdot q \#(S3)$$

$$q = -k \nabla T \#(S4)$$

where E_{in} is the thermal energy input from the solar irradiation; T (x, t) refers to the local temperature; x and t are the space vector and time, respectively; ρ, C_p and k are the mass density, specific thermal capacity, and thermal conductivity of the matters, respectively; u is the fluid flow speed of the aqueous medium.

The theoretical simulation was performed by COMSOL Multiphysics 5.6 under the steady-state analysis mode. The environment temperature was set to 303.15 K, and the heat convection between the upper surface of evaporator and air was corrected by Newton's law of cooling. The thermal conductivity, density, and specific thermal capacity of cotton cloth are 0.0604 W m^{-1} K^{-1}, 75 kg m^{-3}, and 3320 J kg^{-1} K^{-1}, respectively. The thermal conductivity, density, and specific thermal capacity of PCN-700 membrane are 0.0865 W m^{-1} K^{-1}, 100 kg m^{-3}, and 2900 J kg^{-1} K^{-1}, respectively. The thermal conductivity, density, and specific thermal capacity of PS foam are 0.03 W m^{-1} K^{-1}, 30 kg m^{-3}, and 1300 J kg^{-1} K^{-1}, respectively.

Note S4 Analyses of heat loss

Normally, the heat loss of water evaporation process includes radiation, convection, and conduction. Details of the calculation of heat loss are shown as follows,

(1) Radiation

The heat radiation loss was calculated by the Stefan-Boltzmann equation,

$$\emptyset = \varepsilon A\sigma(T_1^4 - T_2^4)\#(S5)$$

where $\emptyset$ represents the heat flux, ε is the emissivity, and the emissivity in the water evaporation processes is supposed to have a maximum emissivity of 1. A is the effective evaporation surface area (615 mm^2). σ is the Stefan-Boltzmann constant (the value is 5.67×10^{-8} W m^{-2} K^{-4}). T_1 is the surface temperature of the as-prepared materials after stable steam generation under one-sun illumination (ca. 55.9 °C, 329.05 K), and T_2 is the ambient temperature upward of the absorber (ca. 42.5 °C, 315.65 K). Then using the following equation to calculate the radiation loss,

$$\eta_{rad} = \emptyset / P_{in}\#(S6)$$

Therefore, the calculated heat radiation loss of the PCN-700 evaporator is 6.3%.

(2) Convection

The convective heat loss is defined by Newton's law of cooling as shown below,

$$Q = hA\Delta T\#(S7)$$

where Q is the convection heat flux, $h$represents the convection heat transfer coefficient, which is approximately 5 W m^{-2} K^{-1}. ΔT is the difference between the surface temperature of the PCN-700 evaporator and the ambient temperature upward the absorber. Consequently, the connection heat loss of the PCN-700 evaporator was calculated through Equation S7, and the value is 6.7%.

(3) Conduction

$$Q = Cm\Delta T\#(S8)$$

where Q is the heat energy, C presents the specific heat capacity of water (4.2 kJ K^{-1} kg^{-1}), and m denotes the weight of water (g). ΔT is the increased temperature of water. In this work, m = 35 g, ΔT = 0.5 K, Consequently, according to Equation S8, the calculated conduction heat loss of PCN-700 evaporator is ca. 3.3%.

Therefore, the heat loss of the PCN-700 evaporator in the water evaporation is ca. 16.3%.

Note S5 Calculation of water evaporation enthalpy

The energy for water to evaporate in dark is gained from the environment, which is therefore the same for different evaporators based on previous work. Considering theoretical evaporation enthalpy of liquid water is ca. 2.434 kJ g^{-1}. Then enthalpy values are obtained as follows,

$$U_{in} = E_{eque} m_g = E_0 m_0 \#(S9)$$

where U_{in} is the total energy absorbed from the environment per hour; E_0 and m_0 refer to the water vaporization enthalpy (2.43 kJ g^{-1}) and the water mass loss (g) of pure water without evaporators in the dark, respectively; E_{eque} is the equivalent evaporation enthalpy of the corresponding system (kJ g^{-1}), and m_g means the corresponding water mass change.

Note S6 Molecular dynamics simulation calculation

The partial charge of GO was calculated using Gaussian 16 code and the 6-311g(d,p) basis functions were applied [32]. The OPLSS-AA force field [33] and Auxiliary Tools of Force Field (AuToFF) were used to parametrize all atoms, such as the bond parameters, angle parameters and the dihedral angles, and so on. The interaction between GO and NaCl solution was studied by molecular dynamics (MD) simulation. 10 GO molecules，89 Na^+ ions, 89 Cl^- ions and 5560 water molecules were randomly inserted into a cube box with a side length of 7.0 nm. The model of water molecule is TIP3P [34]. The MD simulations were performed in the GROMACS 2021 software package [35-37]. The steepest descent method was applied to minimize the initial energy for each system with a force tolerance of 1 kJ mol^{-1} nm^{-1} and a maximum step size of 0.002 ps before MD calculations [38]. In all the three directions, periodic boundary conditions were

imposed. Leapfrog algorithm was used to integrate the Newtonian equation of motion [38]. The MD simulation was processed in an NPT ensemble and the simulation time is 20 ns. In NPT simulations, the pressure was maintained at 1 bar by the Berendsen barostat in an isotropic manner [39]. The temperature was maintained by the V-rescale thermostat at 298.15 K. The LINCS algorithm [40] was performed for constrain bond lengths of hydrogen atoms. The Particle-Mesh-Ewald (PME) with a fourth-order interpolation was used to evaluate the electrostatic interactions and a cutoff of 1.0 nm was employed to calculate the short-range van der Waals interactions [41].

MSD is a statistic describing the random motion of particles, which reflects the average value of the square of the particle's deviation from the initial position and is widely used in molecular dynamics and diffusion research. The *MSD* of molecules is linearly related to the motion time. *D* is used to describe the diffusion rate of matter in the medium, that is, the movement rate of particles from the high concentration area to the low concentration area. The calculation equations of *MSD* and *D* are as follows[42],

$$MSD = \ < |r(t) - r(0)|^2 > \tag{S10}$$

$$D = \lim_{t \to \infty} \frac{1}{6t} < |r(t) - r(0)|^2 > \tag{S11}$$

where < > is the average of all atoms in the group, *t* represents the motion time, and $r(t)$ and $r(0)$ correspond to the displacement of the molecule at *t* and 0 ps, respectively.

Note S7 Calculation of the vapor collection efficiency (condensation efficiency)

Different from evaporation in the open environment, the partial pressure of steam will increase, when a condenser is installed on the evaporation surface to collect steam. The steam partial pressure in the condenser will increase from the initial ambient steam pressure to the saturation pressure, thereby reducing the steam flux. The extent of this decrease of mass flux of vapor would be determined by the condensing capacity of condensers. To measure the condensing capacity of different condensers, the vapor collection efficiency (condensation efficiency, $\eta_{\text{vapor-water}}$) is defined as follows,[43]

$$\eta_{\text{vapor-water}} = m_1 / m_2 \quad \text{(S12)}$$

where m_1 is the mass flux of vapor at the partial pressure of saturated vapor (kg m^{-2} h^{-1}), and m_2 is the mass flux of vapor at the partial pressure of ambient vapor (kg m^{-2} h^{-1}).

References in supporting information

1. B. Chen, J. Ren, Y. Song, P. He, H. Bai, Z. Fan, R. Niu and J. Gong, *ACS Sustainable Chem. Eng.*, 2022, **10**, 16427-16439.
2. N. Liu, L. Hao, B. Zhang, R. Niu, J. Gong and T. Tang, *Energy Environ. Mater.*, 2022, **5**, 617-626.
3. H. Bai, P. He, L. Hao, Z. Fan, R. Niu, T. Tang and J. Gong, *Chem. Eng. J.*, 2023, **456**, 140994.
4. H. Yao, P. Zhang, C. Yang, Q. Liao, X. Hao, Y. Huang, M. Zhang, X. Wang, T. Lin, H. Cheng, J. Yuan and L. Qu, *Energy Environ. Sci.*, 2021, **14**, 5330-5338.
5. P. He, L. Hao, N. Liu, H. Bai, R. Niu and J. Gong, *Chem. Eng. J.*, 2021, **423**, 130268.
6. L. Hao, N. Liu, R. Niu, J. Gong and T. Tang, *Sci. China Mater.*, 2022, **65**, 201-212.
7. X. Chen, C. Meng, Y. Wang, Q. Zhao, Y. Li, X.-M. Chen, D. Yang, Y. Li and Y. Zhou, *ACS Sustainable Chem. Eng.*, 2020, **8**, 1095-1101.
8. Z. Fan, J. Liu, H. Liu, L. Liu, Y. She, X. Wen, H. Wang, G. Hu, R. Niu and J. Gong, *J. Energy Chem.*, 2024, **94**, 527-540.
9. S. Jing, Q. Ji, A. Wang, J. Zhao, H. Liang, F. Chen, P. Kannan and P. Tsiakaras, *Appl. Therm. Eng.*, 2024, **244**, 122629.
10. X. Bai, Q. Wang, M. Tan, P. Zhang, S. Sun, D. Wu, H. Mei, G. Shan, N. Wang, H. Hao, T. Wang and X. Huang, *Chem. Eng. J.*, 2024, **489**, 151441.
11. S. Lal, K. Sundhar and S. K. Batabyal, *Sol. Energy*, 2024, **270**, 112374.
12. S. Luo, Z. Liu, X. Yin, Z. Lin, S. Zhang, J. Chen and M. Guo, *Small*, 2024, **20**, 2309087.
13. Y. Chen, L. Cheng, Q. Liu, M. Chen, C. Li, L. Wang, J. Shen, P. Senin, S. Yan and T. Bian, *Appl. Surf. Sci.*, 2024, **656**, 159667.

14. L. Wang, H. Wang, S. Yu, N. An, Y. Pan, J. Li, T. Jia, K. Wang and W. Huang, *Adv. Funct. Mater.*, 2024, **34**, 2315762.
15. Z. Sui, X. Xue, Q. Wang, M. Li, Y. Zou, W. Zhang and C. Lu, *Carbohydr. Polym.*, 2024, **331**, 121859.
16. Y. Wu, J. Ma, S. Zang, W. Zhou, Z. Wang, M. Han, S. M. Osman, C. Wang, Y. Yamauchi, J. You, M. An, L. Wang and Z. Yuan, *Chem. Eng. J.*, 2023, **472**, 144600.
17. J. Zhang, Z. Li, T. Meng, S. Zang, C. Yang, X. Luo, H. Wang, J. Chen, F. Jing, C. Wang, H. Xu and Y. Zhou, *Chem. Eng. J.*, 2022, **450**, 137893.
18. Z. Fan, J. Ren, H. Bai, P. He, L. Hao, N. Liu, B. Chen, R. Niu and J. Gong, *Chem. Eng. J.*, 2023, **451**, 138534.
19. J. Ren, Y. Ding, J. Gong, J. Qu and R. Niu, *Energy Environ. Mater.*, 2023, **6**, e12376.
20. T. A. Wani, P. Kaith, P. Garg and A. Bera, *ACS Appl. Mater. Interfaces*, 2022, **14**, 35802-35808.
21. X. Che, W. Zhang, L. Long, X. Zhang, D. Pei, M. Li and C. Li, *ACS Nano*, 2022, **16**, 8881-8890.
22. F. Yu, G. Liu, Z. Chen, L. Zhang, X. Liu, Q. Zhang, L. Wu and X. Wang, *ACS Appl. Mater. Interfaces*, 2022, **14**, 40082-40092.
23. X. Zhao, Z. He, W. Ou, P. Lin, Y. Chen and Y. Chen, *Sci. China Mater.*, 2022, **65**, 2491-2501.
24. Z. Sun, C. Han, S. Gao, Z. Li, M. Jing, H. Yu and Z. Wang, *Nat. Commun.*, 2022, **13**, 5077.
25. J. Jiang, H. Jiang, Y. Xu and L. Ai, *Desalination*, 2022, **539**, 115977.
26. H. Liu, L. Liu, Z. Fan, J. Liu, H. Wang, X. Wen, G. Hu, K. Liu, R. Niu and J. Gong, *Chem. Eng. J.*, 2024, **485**, 149690.
27. J. Huang, V. Pereira, C. Wang, H. Li, H. K. Lee and J. Han, *J. Mater. Chem. A*, 2023, **11**, 8110-8118.
28. P. Xiang, C. Tang, K. Ma and X. Li, *Sol. Energy Mater. Sol. Cells*, 2024, **268**, 112750.

29. F. Zhang, Y. Li, H. Cai, Q. Liu and G. Tong, *Carbohydr. Polym.*, 2020, **241**, 116253.
30. Y. Duan, M. Weng, W. Zhang, Y. Qian, Z. Luo and L. Chen, *Energy Convers. Manage.*, 2021, **241**, 114306.
31. C. Ge, D. Xu, H. Du, X. Zhang, Z. Song, H. Zhao, Z. Chen, B. Song, Z. Shen, C. Gao, G. Yan, W. Xu and J. Fang, *Small Methods*, 2023, **7**, 2300227.
32. G. A. Petersson and M. A. Al‐Laham, *J. Chem. Phys.*, 1991, **94**, 6081-6090.
33. W. L. Jorgensen, D. S. Maxwell and J. Tirado-Rives, *J. Am. Chem. Soc.*, 1996, **118**, 11225-11236.
34. W. L. Jorgensen, J. Chandrasekhar, J. D. Madura, R. W. Impey and M. L. Klein, *J. Chem. Phys.*, 1983, **79**, 926-935.
35. D. Van Der Spoel, E. Lindahl, B. Hess, G. Groenhof, A. E. Mark and H. J. C. Berendsen, *J. Comput. Chem.*, 2005, **26**, 1701-1718.
36. M. J. Abraham, T. Murtola, R. Schulz, S. Páll, J. C. Smith, B. Hess and E. Lindahl, *SoftwareX*, 2015, **1-2**, 19-25.
37. H. J. C. Berendsen, D. van der Spoel and R. van Drunen, *Comput. Phys. Commun.*, 1995, **91**, 43-56.
38. W. F. Van Gunsteren and H. J. C. Berendsen, *Mol. Simul.*, 1988, **1**, 173-185.
39. H. J. C. Berendsen, J. P. M. Postma, W. F. van Gunsteren, A. DiNola and J. R. Haak, *J. Chem. Phys.*, 1984, **81**, 3684-3690.
40. B. Hess, H. Bekker, H. J. C. Berendsen and J. G. E. M. Fraaije, *J. Comput. Chem.*, 1997, **18**, 1463-1472.
41. T. Darden, D. York and L. Pedersen, *J. Chem. Phys.*, 1993, **98**, 10089-10092.
42. S. Uehara, I. Hanasaki, Y. Arai, T. Nagai and S. Kawano, *Micro Nano Lett.*, 2014, **9**, 257-260.
43. C. Du and C. Huang, *Appl. Therm. Eng.*, 2022, **201**, 117834.